TOPOLOGICAL DEFECT DETECTION IN ACTIVE NEMATICS USING DEEP CONVOLUTIONAL NEURAL NETWORKS

Ruoshi Liu   *Michael M. Norton*   *Seth Fraden*   *Pengyu Hong*

Brandeis University, Waltham, MA, USA, 02453

ABSTRACT

Active nematics are a class of far-from-equilibrium materials characterized by local orientational order of force-generating, anisotropic constitutes; they include bacterial films, animal cell cultures, and synthetic systems comprised of reconstituted biomolecules. Actively generated stresses induced instabilities that create topological disclinations, local regions of disorder characterized by their winding number. These motile defects, perpetually nucleate and annihilate, exhibiting complex spatiotemporal dynamics. Defect dynamics are influenced by both the material properties of the nematic and boundary conditions; their dynamics can therefore be used as a rheological tool for gaining a deeper understanding of the material. To rapidly and accurately identify defects we developed a novel defect detection technique using deep neural networks. Our approach combines YOLO for fast defect-region proposal and a defect locator built from a two-column deep convolutional neural network. Our approach significantly improves the overall defect detection accuracy and localization when compared to a previously deployed defect detection algorithm that was developed using traditional image processing techniques.

Index Terms— Active Nematics, Topological Defect Detection, Deep Neural Network

1. INTRODUCTION

1.1. Two-Dimensional Confined Active Nematics

Far-from-equilibrium materials are a broad class of internally-driven, energy-consuming systems studied by the soft condensed matter community. An important subclass are active nematic materials. Passive nematic liquid crystals are well known for their use in display technologies and are comprised of elongated constituent molecules that exhibit high orientational order [1]. Nematics can contain localized regions of orientational disorder known as defects (Fig. 1) that are named according to their topological winding number [2]. In the absence of driving forces, defects in a nematic will anneal over time through molecular reorientation. By contrast,

the constituents of far-from-equilibrium nematics such as cell cultures [3, 4], bacterial suspensions [5, 6], filamentous biofilms [7], synthetic microtubule-based materials [8, 9] and others [10, 11] possess internal stresses that spontaneously produce topological defects through dynamic instabilities that produce ±1/2 defect pairs. Active stress imbues each defect type with unique dynamics (Fig. 1): the comet-shaped +1/2 defects are self-propelling while the three-fold symmetry of the -1/2 defects creates an active flows that result in no net translation of the structure.
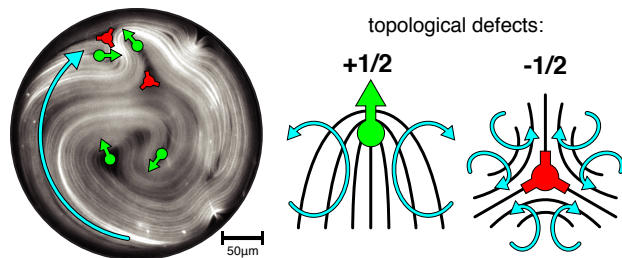
Fig. 1: **Left:** Fluorescently labeled active microtubule suspension confined to a 300 μm well. Topological defects with $+\frac{1}{2}$ and $-\frac{1}{2}$ defects labeled by green arrows and red dots with three prongs, respectively. The material circulate clock-wise (cyan arrow). **Right:** Schematic representation of topological defects and their idealized active flows (cyan arrows) [10, 11].

Experimental observations [9, 12, 13, 14] and theoretical predictions [15, 16] show that hydrodynamic interactions between defects gives rise to striking spatio-temporal dynamics in the form of nucleation and annihilation, and complex trajectories. Geometric confinement greatly influences these dynamics, and can tame the otherwise turbulent flows into system-sized vortices that exhibit complex periodic patterns [14]. In order to characterize these dynamical structures and derive theories to describe them, researchers need to analyze a huge volume of videos of active nematics to detect and trace patterns (e.g., ±1/2 defects), which is prohibitively time consuming. Hence, an automatic tool for rapid and robust defect detection is essential.

In this work, we developed a deep neural network based approach on fluorescence microscopy images of an extensile active nematic system, which is composed of microtubules and motor proteins in circular disks [8, 9, 14]. Our approach

is applicable to other nematic materials.

1.2. Traditional Defect Detection Algorithm

We previously developed a two-step analysis method using traditional image processing techniques. First, the director field tangent to microtubule bundles is identified. This field can be measured directly using polscope microscopy [9] or computed through image processing [14]. In the latter, the image gradient is calculated and the principal components of the second rank tensor $G = \nabla I \otimes \nabla I$ are extracted for every pixel. The eigenvector associated with the smallest eigenvalue corresponds to the local direction of the microtubule fibers $\mathbf{n}$. In the second step, the signed winding number $w = \frac{1}{2\pi} \oint \frac{\partial \theta}{\partial \mathbf{x}} \cdot d\mathbf{x}$ (where $\theta = \tan^{-1}(n_y/n_x)$), is calculated over all image regions using a pre-defined window-size [2]. The integral is identically zero unless the director field contains a singular point [9, 12]. This algorithm performs reasonably well in detecting both ±1/2 defects; however, performance depends on the quality of the director field that can be extracted. In practice, the field is an imperfect representation of the microtubule orientation. Overexposed regions, unfocused regions, and microtubule material extending beyond the confinement plane are common challenges that lead to false positives and false negatives. While careful filtering of the director field can ameliorate these issues, this requires dataset-dependent tuning and long processing time.

2. METHODS
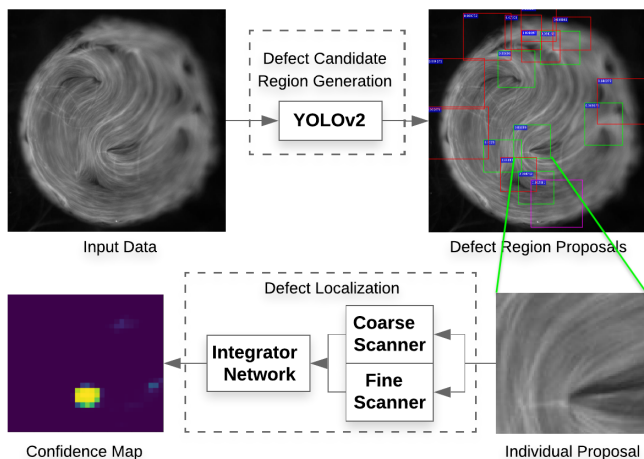
Fig. 2: The proposed two-stage defect detection system. In the first stage, a YOLO model is trained to propose candidate defect-containing regions. In the second stage, two CNNs (coarse and fine scanners) are integrated to accurately detect defects in the regions proposed by YOLO.

The task of defect detection is special in the sense that defects are singular points in an image with no clear boundaries. Because of this characteristic, existing object detection techniques tend to localize defects poorly. Therefore, we developed a two-stage approach [Fig. 2]. The 1st stage trains a YOLO model [17] for quickly proposing the rough defect-containing regions in an image. Several similar models have been developed in the recent years including R-CNN [18, 19] and SSD [20]. We chose YOLO because it produced much fewer false positives in our data and is the fastest among all state-of-the-art methods. In the 2nd stage, a two-column convolutional neural network (CNN) is trained to accurately localize defects in the regions proposed by the YOLO model. Each column is a CNN. One of them (Coarse Scanner) is trained to distinguish defects from general non-defect regions, and the other one (Fine Scanner) is trained to differentiate defects from their vicinities. The output of the two-column CNN will be integrated by an Integrator Network trained to optimize the prediction of defect locations.

2.1. Training & Testing Data

We manually labeled the positions of ±1/2 defects in 8300 images from 9 experimental videos, and divided them randomly into 6600 for training, 567 for validation, 1133 for testing (samples of training and testing data are included in supplementary materials). The location of a +1/2 defect is labeled at the point where the orientation of the materials change the most sharply, and the location of a -1/2 defect is labeled at the center of its triangular material-devoid region (Fig. 1). The size of +1/2 defects vary significantly. For example, in Fig. 3, there are four +1/2 defects, with defect 1 appearing drastically different (much bigger than) from defects 2-4. The regular bounding box used for defining most +1/2 defects is too small to cover defect 1. Hence, we created a separate class for "open" +1/2 defects like defect 1 in Fig. 3 and gave it a bigger bounding box (1/3 bigger than other classes).
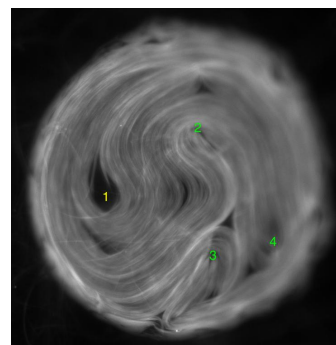
Fig. 3: Varying sizes of +1/2 defects. Defect 1 is an "open" +1/2 defect that is much larger than other "closed" +1/2 defects 2, 3, 4.

Due to the topological constraints imposed by parallel alignment of the nematic along the boundary [2], the system maintains a total topological charge of +1, which requires exactly two more +1/2 defects than -1/2 defects in each frame, leading to unbalanced training data. Specifically, our training set possesses 58536 samples of +1/2 defect and 24518 sam-

ples of -1/2 defect. To address this issue and also increase model robustness, we adopted several data augmentation techniques: 1) random rotation; 2) random horizontal and vertical flipping; 3) Gaussian noises, salt pepper noises, and speckle noises. In addition, a circular mask was applied to black out fringe region (devoid of materials) of a defect bounding box.

2.2. Improve Defect Localization

In the prediction results of YOLO, we observed poor localization performance manifested by drastically shifting bounding boxes across consecutive frames in a video. Moreover, in the predicted bounding boxes containing defects, the distances between defect locations to the centers of the bounding boxes are large (summarized in Fig. 6). To more precisely locate defects, we trained a Defect Locator – a two-column deep neural network composed of two CNNs integrated by a subnetwork with 2 fully-connected layers (see the network within the dash rectangle in the bottom of Fig. 2). The Defect Locator is used to scan each region proposed by YOLO to produce a confidence map of defects whose local maxima are extracted as the defect locations. Because the varying sizes of nematic systems and image resolutions, we use the normalized distance (i.e., the portion of the image size) to report the localization results unless otherwise noted in the rest of the paper. For example, a normalized distance of 0.075 is around 52 pixels in a typical 700×700 image.

2.2.1. Training the Defect Locator

The two CNNs in the Defect Locator were trained to distinguish 4 classes: "closed" +1/2 defects, "open" +1/2 defects, -1/2 defects, backgrounds (i.e., image regions whose center areas are not defects). Both CNNs are ResNet-34 [21]. They were trained differently in how their background training data was chosen. The background training data of the 1st CNN were sampled uniformly from the whole image (excluding those within 0.02 normalized distance to defects), which trains the 1st CNN to eliminate most non-defect-containing regions. Hence, we name this CNN the Coarse-Scanner. The background training data of the 2nd CNN was sampled in the vicinity of defects (within 0.02-0.07 normalized distance to defects), which was used to train the 2nd CNN to determine if a region has a defect close to its center. We name the 2nd CNN as the Fine-Scanner. The outputs of both CNNs are then integrated by a three-layer fully connected network. ReLU [22] was used in the first two hidden layers (each layer contains 100 neurons), and softmax was used in the output layer containing four neurons.
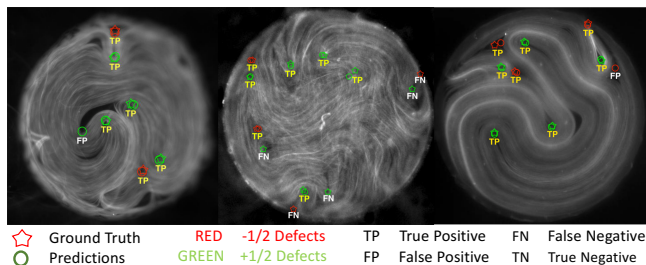
To deal with unbalanced training data, equal number of "closed" +1/2 defects, "open" +1/2 defects, -1/2 defects and background regions were sampled to train the Fine-Scanner in each epoch. In each training epoch of the Coarse-Scanner, since the background set is much larger than the defect sets,

we randomly sampled backgrounds to be four times the amount of the rest classes, and adjusted the weights in loss function to 1:1:1:4 for "closed" +1/2 defect, "open" +1/2 defect, -1/2 defect, and background, respectively. Both Coarse-/Fine-Scanners were trained using Adam [23] to minimize the cross-entropy loss function with a L2 regularization at the level of 1e-5. Initial learning rates was 0.00025, which was reduced by half every 100 epochs. After training the Coarse-/Fine-Scanners, we froze their parameters and fed their outputs to train the Integrator subnetwork. In each epoch, the defect training data was sampled in the same manner to the above, while the background data was sampled from bounding boxes generated by YOLO but not within a 0.02 normalized distance to defects. When training the Integrator subnetwork, Stochastic Gradient Decent with Momentum was used to minimized the cross-entropy loss. The initial learning rate was 0.01 and was reduced by half every 10 epochs. The total number of training epochs is 50.

We used the validation test to tune the confidence threshold of our YOLO model to obtain a high recall rate (89.9%). During detection, an input image is first filtered by the trained YOLO model to generate multiple bounding boxes. Each of these bounding boxes is then scanned in parallel by the Defect Locator to extract the locations of defects. A fix window size of 0.045 normalized distance and a stride number of 2 are used for slide-window scanning to produce a confidence map.

3. EXPERIMENTAL RESULTS

3.1. Detection Performance

| ☆ Ground Truth | RED -1/2 Defects | TP True Positive | FN False Negative |
| ○ Predictions | GREEN +1/2 Defects | FP False Positive | TN True Negative |

Fig. 4: Exemplar test results of our approach. The predictions and ground truth are labeled in circles and pentagrams, respectively. The +1/2 and -1/2 defects are labeled in green and red, respectively.

The performance of our approach was evaluated by recall, precision and F2-score, and was compared with those of the traditional method and the YOLO alone method in Table 1. We considered a prediction to be correct if there was a defect of the same class within a normalized distance of 0.075. When tuning our 2-stage approach and the YOLO alone method, we used the validation test to select the thresholds on the LogSoftMax outputs to maximize their F2-scores in validation. The traditional approach needed to be fine-tuned manually for each video using several of its carefully

	Traditional	**YOLO**	**Ours**
precision +1/2	**0.881**	0.784	0.831
recall +1/2	0.601	**0.845**	0.815
F2-score +1/2	0.714	0.813	**0.823**
precision -1/2	0.361	0.402	**0.591**
recall -1/2	**0.762**	0.396	0.555
F2-score -1/2	0.490	0.399	**0.572**
F2-score overall	0.637	0.688	**0.749**

Table 1: Compare the defect detection performances of the traditional method, YOLO, and our approach. Defect types are indicated by +1/2 and -1/2.

chosen representative frames. Table 1 shows that our approach leads the other two approaches in all F2-score measurements. Sample test videos with defect annotations and detection results are included in supplementary materials.

As shown in Fig. 5, all methods performed less accurately in the area close to the boundary of the confining disk. We believe the poor performances of our approach and the YOLO-alone method were due to the following reasons. (1) Defects appear less frequently in the outer region. For example, in our data, only about 22% defects are located at the outer regions. The outer region has the largest area but contains the least number of defects. The lower detection performance is expected because of relatively insufficient number of training samples. (2) Nucleation and annihilation happen more often near the boundary, and hence make it harder to detect defects. (3) Defects near the boundary are smaller in size and less clear in appearance with high variations.
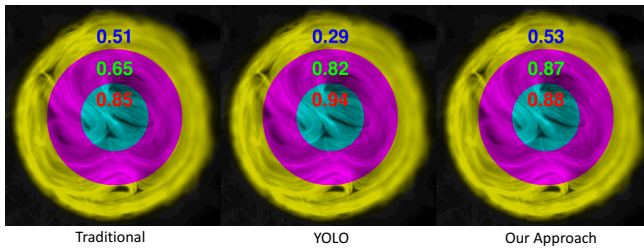
Fig. 5: Compare the F2-scores in three different regions (outer-yellow, middle-red, and inner-green) of the test images. YOLO indicates the YOLO-alone method.

### 3.2. Defect Localization Test

We also compared the localization performances of our approach, the YOLO-alone method, and the traditional algorithm (see Figure 6). The defect location detected by the YOLO-alone method was calculated as the center of the corresponding rectangle. A normalized distance of 0.075 is used to decide if a detection is within a correct range of the ground truth. Our approach performed significantly better than two other approaches.
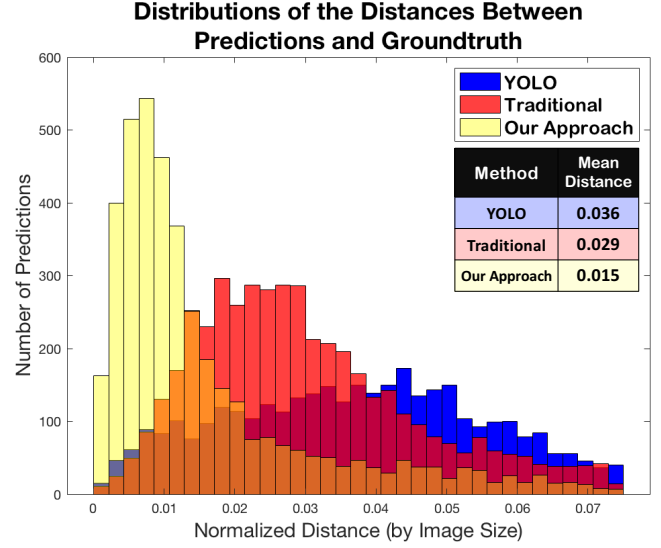
Fig. 6: Compare localization performances. YOLO indicates the YOLO-alone method.

4. CONCLUSION AND DISCUSSION

Our deep-learning based approach outperformed the traditional approach in both detection accuracy and localization. Once trained, our model can be robustly applied to new data without needing to fine-tune for individual datasets. The significant improvement in localizing defects will greatly facilitate quantifying active nematic dynamics. We observed that our detection mistakes happened more often during the nucleation or annihilation of a defect (see Fig. 7). Identifying the exact frame when a defect nucleates or annihilates is challenging even for human annotators. We will improve our method in the future by increasing training data and/or expanding our model to include a subnetwork to handle this special category. Recently, experimental data from 3D active nematics has been collected in which topological defects are lines and loops instead of singularity points as in 2D nematic systems. Robust 3D defect detection method is urgently needed. More generally, many experiments in the field of soft matter involve identifying patterns (objects) in images/videos. Our work demonstrates that deep-learning is a viable approach to analyze these experimental data.
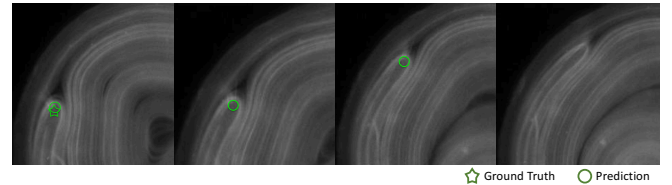
Fig. 7: The annihilation process of an +1/2 defect. In the 1st and last frames, our detection results match the manual annotations. In the 2nd and 3rd frames, our approach detected a +1/2 defect which however was not manually confirmed.

5. REFERENCES

[1] Pierre-Gilles de Gennes and J. Prost, *The Physics of Liquid Crystals*, Oxford University Press, 1995.

[2] Randall D Kamien, "The geometry of soft materials: a primer," *Reviews of Modern physics*, vol. 74, no. 4, pp. 953, 2002.

[3] G. Duclos, S. Garcia, H. G. Yevick, and P. Silberzan, "Perfect nematic order in confined monolayers of spindle-shaped cells," *Soft Matter*, vol. 10, no. 14, pp. 2346–2353, 2014.

[4] Guillaume Duclos, Christoph Erlenkämper, Jean François Joanny, and Pascal Silberzan, "Topological defects in confined populations of spindle-shaped cells," *Nature Physics*, vol. 13, no. 1, pp. 58–62, 2017.

[5] H. Wioland, E. Lushi, and R. E. Goldstein, "Directed collective motion of bacteria under channel confinement," *New Journal of Physics*, vol. 18, no. 7, pp. 075002, jul 2016.

[6] He Li, Xia-Qing Shi, Mingji Huang, Xiao Chen, Minfeng Xiao, Chenli Liu, Hugues Chaté, and H P Zhang, "Data-driven quantitative modeling of bacterial active nematics," *Proceedings of the National Academy of Sciences*, vol. 33, pp. 201812570, dec 2018.

[7] Yusuf Ilker Yaman, Esin Demir, Roman Vetter, and Askin Kocabas, "Emergence of active nematics in bacterial biofilms," vol. 168, 2018.

[8] G. Henkin, S. J. DeCamp, D. T. N. Chen, T. Sanchez, and Z. Dogic, "Tunable dynamics of microtubule-based active isotropic gels," *Philosophical Transactions of the Royal Society A: Mathematical, Physical and Engineering Sciences*, vol. 372, no. 2029, pp. 20140142–20140142, 2014.

[9] Stephen J. DeCamp, Gabriel S. Redner, Aparna Baskaran, Michael F. Hagan, and Zvonimir Dogic, "Orientational order of motile defects in active nematics," *Nature Materials*, vol. 14, no. 11, pp. 1110–1115, aug 2015.

[10] M. C. Marchetti, J. F. Joanny, S. Ramaswamy, T. B. Liverpool, J. Prost, Madan Rao, and R. Aditi Simha, "Hydrodynamics of soft active matter," *Reviews of Modern Physics*, vol. 85, no. 3, pp. 1143–1189, 2013.

[11] Amin Doostmohammadi, Jordi Ignés-Mullol, Julia M. Yeomans, and Francesc Sagués, "Active nematics," *Nature Communications*, vol. 9, no. 1, pp. 3246, 2018.

[12] Perry W. Ellis, Daniel J.G. G Pearce, Ya-Wen Wen Chang, Guillermo Goldsztein, Luca Giomi, and Alberto Fernandez-Nieves, "Curvature-induced defect unbinding and dynamics in active nematic toroids," *Nature Physics*, vol. 14, no. 1, pp. 85–90, 2018.

[13] Pau Guillamat, Jordi Ignés-Mullol, and Francesc Sagués, "Taming active turbulence with patterned soft interfaces," *Nature Communications*, vol. 8, no. 1, pp. 1–8, 2017.

[14] Achini Opathalage, Michael M Norton, Michael PN Juniper, S Ali Aghvami, Blake Langeslay, Seth Fraden, and Zvonimir Dogic, "Self-organized dynamics and the transition to turbulence of confined active nematics," *arXiv preprint arXiv:1810.09032*, 2018.

[15] Amin Doostmohammadi, Sumesh P. Thampi, and Julia M. Yeomans, "Defect-Mediated Morphologies in Growing Cell Colonies," *Physical Review Letters*, vol. 117, no. 4, 2016.

[16] Michael M. Norton, Arvind Baskaran, Achini Opathalage, Blake Langeslay, Seth Fraden, Aparna Baskaran, and Michael F. Hagan, "Insensitivity of active nematic liquid crystal dynamics to topological constraints," *Physical Review E*, vol. 97, no. 1, pp. 1–8, 2018.

[17] Joseph Redmon, Santosh Divvala, Ross Girshick, and Ali Farhadi, "You only look once: Unified, real-time object detection," in *The IEEE Conference on Computer Vision and Pattern Recognition (CVPR)*, June 2016.

[18] Ross Girshick, "Fast r-cnn," in *Proceedings of the IEEE international conference on computer vision*, 2015, pp. 1440–1448.

[19] Shaoqing Ren, Kaiming He, Ross Girshick, and Jian Sun, "Faster r-cnn: Towards real-time object detection with region proposal networks," in *Advances in neural information processing systems*, 2015, pp. 91–99.

[20] Wei Liu, Dragomir Anguelov, Dumitru Erhan, Christian Szegedy, Scott Reed, Cheng-Yang Fu, and Alexander C Berg, "Ssd: Single shot multibox detector," in *European conference on computer vision*. Springer, 2016, pp. 21–37.

[21] Kaiming He, Xiangyu Zhang, Shaoqing Ren, and Jian Sun, "Deep residual learning for image recognition," in *The IEEE Conference on Computer Vision and Pattern Recognition (CVPR)*, June 2016.

[22] Xavier Glorot, Antoine Bordes, and Yoshua Bengio, "Deep sparse rectifier neural networks," in *Proceedings of the fourteenth international conference on artificial intelligence and statistics*, 2011, pp. 315–323.

[23] Diederik P Kingma and Jimmy Ba, "Adam: A method for stochastic optimization," *arXiv preprint arXiv:1412.6980*, 2014.